Article

Adaptive Visual Saliency Feature Enhancement of CBCT for Image-Guided Radiotherapy

Lisiqi Xie, Kangjian He and Dan Xu *

School of Information Science and Engineering, Yunnan University, Kunming 650500, China;
hekj@ynu.edu.cn (K.H.)
* Correspondence: danxu@ynu.edu.cn

Abstract: Unlike the high imaging radiation dose of computed tomography (CT), cone-beam CT (CBCT) has smaller radiation dose and presents less harm to patients. Therefore, CBCT is often used for target delineation, dose planning, and postoperative evaluation in the image-guided radiotherapy (IGRT) of various cancers. In the process of IGRT, CBCT images usually need to be collected multiple times in a radiotherapy stage for postoperative evaluation. The effectiveness of radiotherapy is measured by comparing and analyzing the registered CBCT and the source CT image obtained before radiotherapy. Hence, the registration of CBCT and CT is the most important step in IGRT. CBCT images usually have poor visual effects due to the small imaging dose used, which adversely affects the registration performance. In this paper, we propose a novel adaptive visual saliency feature enhancement method for CBCT in IGRT. Firstly, we denoised CBCT images using a structural similarity based low-rank approximation model (SSLRA) and then enhanced the denoised results with a visual saliency feature enhancement (VSFE)-based method. Experimental results show that the enhancement performance of the proposed method is superior to the comparison enhancement algorithms in visual objective comparison. In addition, the extended experiments prove that the proposed enhancement method can improve the registration accuracy of CBCT and CT images, demonstrating their application prospects in IGRT-based cancer treatment.

Keywords: cone beam CT; feature enhancement; low-rank approximation; image-guided radiotherapy

1. Introduction

The purpose of radiotherapy is to deliver a planned radiation dose to a delineated cancerous region to kill cancer cells while preserving the surrounding normal structures and leaving tissues unharmed [1–3]. It is very difficult to accurately radiate the target region and ensure the surrounding normal areas are not damaged [4,5]. Image-guided radiotherapy (IGRT) is a new cancer treatment technology in which images are used to guide the whole radiation process including position guidance, pre-operative and postoperative analysis [6–8]. The key step of IGRT is to collect and analyze CT and CBCT images of the target area. High-quality CT images only need to be collected a few times for diagnosis and treatment planning, and CBCT images need to be collected many times for patient positioning guidance during the radiotherapy. CBCT imaging is used to replace CT imaging as much as possible to reduce the harm caused by the high dose of CT to patients. When IGRT-based treatment is implemented, some image technologies need to be used to supervise and guide the whole treatment process. Due to this process often requiring multiple acquisitions and analyses of images, CBCT, with its lower imaging dose, is usually used as the guidance image to reduce the harm to the patient [9,10]. In IGRT, the most important step is to analyze the position information between the CBCT image and the delineated CT images; that is, the radiologist needs to register and align the CBCT and the CT images.

As shown in Figure 1, CBCT images usually have low contrast and visual quality due to their small imaging dose compared with CT images. Compared with CT, CBCT has

a small imaging dose, which means that its imaging is more susceptible to interference from environments such as a strong magnetic field, resulting in more noise in the CBCT image. The degradation of CBCT will reduce image contrast and increase the ambiguity of structures of important regions, which makes it unable to play its due role in IGRT [11]. Huang et al. proved that the accuracy of radiotherapy can be improved by using CBCT enhancement technology in IGRT [12]. Thus, it has become a new research topic to use image enhancement technology to improve the quality of CBCT.
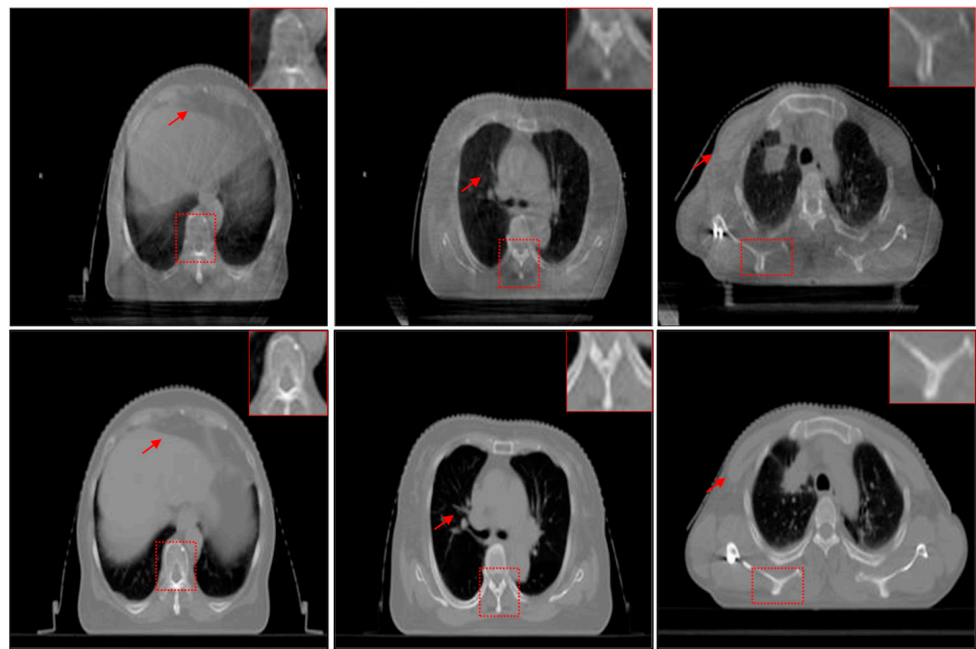

Figure 1. Examples of unregistered CBCT (the first row) and CT (the second row) images.

In recent decades, different types of efficient methods have been proposed for image enhancement [13–15], such as the well-known histogram equalization (HE) method [16], dark channel prior (DCP) method [17], signal scale retinex (SSR) method [18], multiscale retinex with color restoration (MSRCR) method [19], semi-decoupled decomposition (SSD) method [20], and statistical methods with image processing concepts (SMIPC) [21]. Among them, HE is a classical image enhancement algorithm, which mainly improve the visual quality by calculating and adjusting the distribution of pixel values and increasing the gray level difference of the input image. The DCP method assumes that the image is degraded during the imaging process and then calculates a transmission map to estimate the degradation to enhance the degraded image. The DCP method has better performance in foggy image enhancement. SSR and MSRCR are typical methods based on retinex theory. SSR is a single-scale retinex algorithm, which achieves enhancement by establishing an illumination reflection model in the imaging process and performing high-frequency enhancement processing on the reflected component. MSRCR is a multi-SSR-based algorithm with a color restoration factor to adjust the contrast of the input image and improve the color information. SSD is a Gaussian total variation model performing retinex decomposition in a semi-decoupled fashion for simultaneous brightness enhancement and noise suppression. SMIPC-based methods enhance the contrast of medical images using statistical methods with image processing concepts. Although the above enhancement methods have their own advantages for different types of images, most of them ignore an important point for medical image enhancement, especially for CBCT images: the medical images may contain noise due to the interference of the surrounding environment [22]. Based on this motivation, we propose an adaptive visual saliency feature enhancement method of CBCT for image-guided radiotherapy, which takes the denoising process into account to overcome the influence of potential noise on the enhancement results. First, we propose a structural

similarity-based low-rank approximation model (SSLRA) to construct the source CBCT images to denoise the noise that may exist. Low-rank approximation (LRA) is an extension of singular value decomposition (SVD) in machine learning. Unlike in our previous work [23], we propose an unsupervised adaptive denoising model based on structural similarity considering the characteristics of CBCT images. Then, we propose a visual saliency feature-based enhancement (VSFE) method to enhance the important regions in CBCT images.

The main contributions of this work are as follows: (1) A novel unsupervised adaptive denoising model called a structural similarity-based low-rank approximation (SSLRA) model is proposed for CBCT images. (2) A visual saliency feature enhancement (VSFE) method is proposed, in which more salient and important regions of CBCT can be enhanced. (3) By analyzing the support for subsequent registration tasks of CBCT and CT, we prove that the proposed method can effectively improve the registration performance, indicating its application prospects in IGRT.

The rest of this paper is organized as follows. Section 2 describes the proposed method in detail. Experimental results and analyses are presented in Section 3. Section 4 discusses the application of our work in IGRT. Section 5 gives the conclusion of our work.

2. Materials and Methods

We propose a novel adaptive visual saliency feature enhancement of CBCT for image-guided radiotherapy in this section. As shown in Figure 2, the proposed method consists of two steps: structural similarity-based low-rank approximation for denoising, and the visual saliency feature enhancement for improving detail.
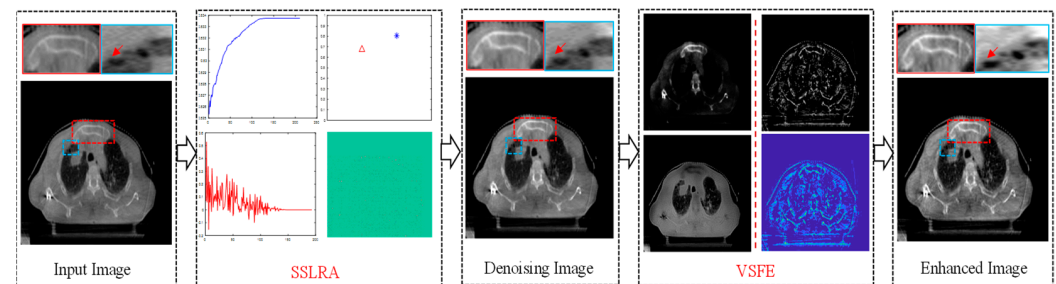

Figure 2. Flowchart of the proposed method for CBCT image enhancement method, in which SSLRA denotes the proposed structural similarity-based low-rank approximation algorithm and VSFE denotes the proposed visual saliency feature based enhancement algorithm.

2.1. Structural Similarity-Based Low-Rank Approximation

Based on the singular value decomposition (SVD) algorithm [24–27], we propose a structural similarity-based low-rank approximation method (SSLRA) to reconstruct the input CBCT images so as to denoise the source image. The decomposition and reconstruction of the SVD of an image **X** with size $m \times n$ can be expressed as:

$$\mathbf{X} = U \sum V^T \tag{1}$$

where $\mathbf{X} \in \mathbb{R}^{m \times n}$, $U \in \mathbb{R}^{m \times m}$, $\sum \in \mathbb{R}^{m \times n}$, and $V \in \mathbb{R}^{n \times n}$; the columns of the $m \times n$ matrix U are the left singular vectors; and the rows of the $n \times n$ matrix V^T contain the elements of the right singular vectors. $\sum$ is the diagonal matrix, where $\sum = (\sum_n, \mathbf{0})$ and $\sum_n = diag(\sigma_1, \cdots, \sigma_n)$. In addition, $\sigma_k > 0$ if $1 \leq k \leq r$ and $\sigma_k = 0$ if $r + 1 \leq k \leq n$, where r is the rank of **X**. Using Equation (1), the source image can be computed by three matrices. Then, the image **X** can be reconstructed by:

$$\mathbf{X} = \sigma_1 u_1 v_1^T + \sigma_2 u_2 v_2^T + \cdots + \sigma_r u_r v_r^T \tag{2}$$

where u and v are the left singular vectors and right singular vectors in U and V, respectively, and σ is the singular value in $\sum$.

The reconstruction result $\mathbf{X}_p$ of different features can be obtained by:

$$\mathbf{X}_p = \sum_{i=1}^{p} \sigma_i u_i v_i^T \tag{3}$$

where $1 \le p \le r$. When $p = r$, the full rank reconstruction result is $\mathbf{X}_p = \mathbf{X}$. That is, the denoised $\mathbf{X}_p$ can be estimated from $\mathbf{X}$ by solving:

$$\mathbf{X}_p = \underset{\mathbf{Z}}{\arg\min} \|\mathbf{X} - \mathbf{Z}\|_F^2 \text{ s.t. rank}(\mathbf{Z}) = \text{k} \tag{4}$$

where $\text{rank}(\cdot)$ denotes the rank of the given data.

Equation (4) can be solved by the theorem of Eckart–Young–Mirsky. That is, for the given matrix $\mathbf{A}$ with $k < r = rank(\mathbf{A})$, the truncated matrix can be expressed by:

$$\mathbf{A}_k = \sum_{i=1}^{k} \sigma_i u_i v_i^T \tag{5}$$

Next, for any given matrix $\mathbf{B}$ with rank k, the minimal error can be computed with $\mathbf{A}_k$:

$$\min_{rank(\mathbf{B})=k} = \|\mathbf{A} - \mathbf{B}\|_2 = \|\mathbf{A} - \mathbf{A}_k\|_2 = \sigma_{k+1} \tag{6}$$

The above Equations shows that $\mathbf{A}_k$ can be as the optimal solution of $\mathbf{A}$ in the Frobenius norms sense. That is, Equation (6) can be computed by:

$$\min_{rank(\mathbf{B})=k} = \|\mathbf{A} - \mathbf{B}\|_F = \|\mathbf{A} - \mathbf{A}_k\|_F = \sum_{i=k+1}^{r} \sqrt{\sigma_i^2} \tag{7}$$

By an optimal rank, the reconstruction result can be denoised with high imaging quality and more detailed information.

The proposed SSLRA are summarized in Algorithm 1, in which $SS(\cdot)$ is defined as:

$$SS(I,J) = ((2\mu_I \mu_J + C_1)(2\sigma_{IJ} + C_2))/((\mu_I^2 + \mu_J^2 + C_1)(\sigma_I^2 + \sigma_J^2 + C_2)) \tag{8}$$

where μ_I, μ_J are the local means of image I and J. σ_I, σ_J and σ_{IJ} are the standard deviations and cross-covariance of I and J. $W_{mc}(I_p)$ can be computed by:

$$W_{mc}(I_p) = 2\|\nabla U\|_2 H(U) \tag{9}$$

where ∇ is the gradient operator. Equation (9) is derived from total variation (TV) regularization. For an image U, the mean curvature of U is:

$$H(U) = \frac{1}{2} \nabla \cdot \frac{\nabla U}{\|\nabla U\|_2} = \frac{U_x^2 U_{yy} - 2U_x U_y U_{xy} + U_y^2 U_{xx}}{2(U_x^2 + U_y^2)^{\frac{3}{2}}} \tag{10}$$

More details about Equation (10) can be found in our previous work [17].

Algorithm 1 Structural similarity based low-rank approximation (SSLRA)

Input: CBCT image I
Output: Denoised image I_D
1.   **for** $k = 1$ to r **do**
2.   Compute $S(k) = SS(I, I_k - W_{mc}(I_k))$
3.   Compute $R(k) = \partial S(k)/\partial k, 1 \leq k \leq r$
4.   **while** $R(k) \neq 0$ **do**
5.   Update $I_k, R(k)$
         end while
6.   **end for**
7. $R_{opt} = \begin{cases} k, \ if \, R(k) = 0 \text{ for the first time} \\ r, \ otherwise \end{cases}$
8.   Reconstruct by Equation (3) with R_{opt}
9.   **return:** I_D

Two examples of SSLRA are given in Figure 3. Figure 3a is the source CBCT image, and Figure 3b,c are the normalized curves of $S(p)$ and $R(p)$, respectively. Figure 3d is the reconstructed image, and Figure 3e is the difference image between Figure 3a,d. From the difference image, it can be found that the proposed SSLRA method suppresses some discrete noise points during the reconstruction process. This is necessary for the next step of detail enhancement, and denoising using the proposed SSLRA first will avoid enhancing the noise that may exist in these source CBCT images.
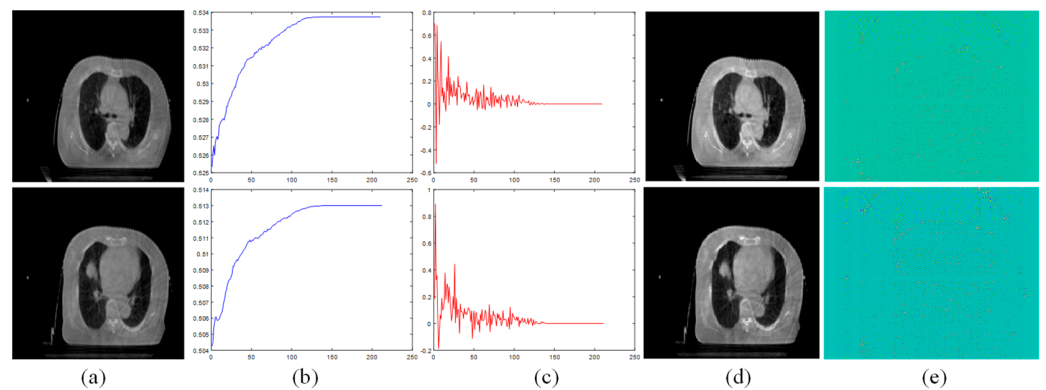

(a)	(b)	(c)	(d)	(e)

Figure 3. Illustration of SSLRA. (**a**) Source CBCT images. (**b**) Normalized curves of $S(k)$. (**c**) Normalized curves of $R(k)$. (**d**) Reconstructed images. (**e**) Difference maps between (**a**,**d**).

2.2. Visual Saliency Feature-Based Enhancement

Visual saliency detection is used to make the region of our interest stand out more from its neighbors and surrounding pixels [28]. Some existing visual saliency detection methods highlight the edges and textures of the entire salient region. The saliency map can be obtained by computing the Euclidean distance in CIELab color space as follows:

$$S(i,j) = \left\| I_\mu - I_f(i,j) \right\| \tag{11}$$

where I_μ is the average pixels of the input image in CIELab color space and $S(i,j)$ is the computed significance value at (i,j). $I_f(i,j)$ is the corresponding pixel in the Gaussian blurred image of the input image, and $\|\cdot\|$ denotes the L_2 norm. However, these methods compute the difference between the average pixels of the entire input image and its corresponding blurred version and often fail to maintain good performance when the input image has a noisy background or the imaging scene is large. Achanta et al. [29] proposed a maximum symmetric surround-based saliency detection method. For an input image

with size $m \times n$, the symmetric surround saliency value at the given pixel $S_{SS}(i,j)$ can be computed as:

$$S_{SS}(i,j) = \left\| I_\mu(i,j) - I_f(i,j) \right\| \tag{12}$$

where $I_\mu(i,j)$ is the average pixels of the sub-image centered at pixel (i,j) in CIELab color space and computed as:

$$I_\mu(i,j) = \frac{1}{A} \sum_{x=i-i_o}^{i+i_o} \sum_{y=j-j_o}^{j+j_o} I(x,y) \tag{13}$$

where i_o, j_o is the local window size, and the area A of the sub-image is determined by:

$$A = (2i_o + 1)(2j_o + 1). \tag{14}$$

When the visual saliency detection results are obtained by Equation (12), the salient region of the input image will be stretched and enhanced, as shown in Figure 4.

In the proposed VSFE algorithm, the saliency detection result from Equation (12) will be used as the visual saliency decision map for further detail enhancement. The visual saliency enhancement can be computed by:

$$I_{VSE} = I_R + \alpha S_{SS}(I_R) \cdot I_R \tag{15}$$

where α is the enhancing weight parameter, I_R is the reconstructed result by the SSLRA, and $S_{SS}(I_R)$ is the visual saliency map of I_R.

Some examples of I_{VSE} are given in Figure 5c. Compared with the reconstructed results in Figure 5b, the contrast of the visual saliency enhancement images is higher and the important regions are easier to observe.
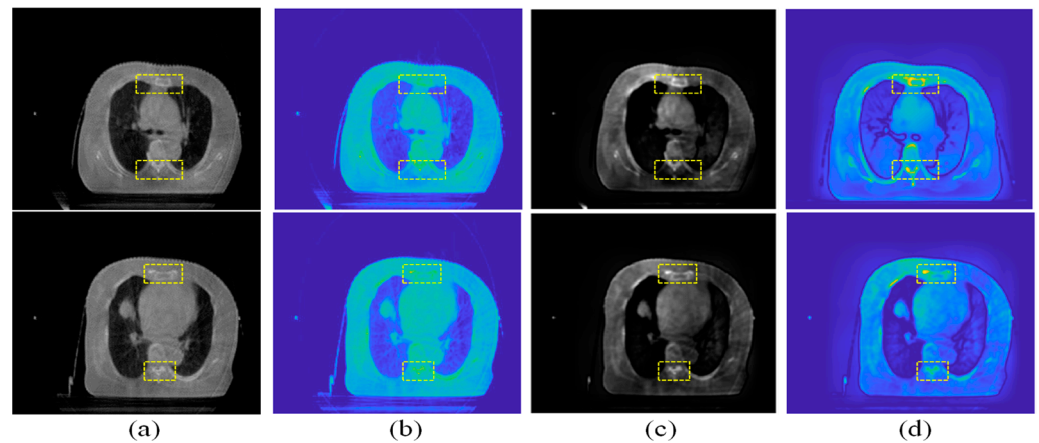

Figure 4. Examples of visual saliency detection. (**a**) Source CBCT images. (**b**) Pseudo-color image of (**a**). (**c**) Saliency map of (**a**). (**d**) Pseudo-color image of (**c**).

It can be found that I_{VSE} only enhances the salient features, and in the next step, we perform the overall detail enhancement on the images to further improve their quality. To enhance detail, the mutually guided image filter (MuGIF) method is adopted in the proposed VSFE algorithm. The MuGIF can be used to extract the relative structure of two images and the structure information of a single image [30–32]. The related structure of **T** and **R** of MuGIF is defined as:

$$\mathcal{R}(\mathbf{T},\mathbf{R}) = \sum_i \sum_{d \in \{h,v\}} \frac{|\nabla_d \mathbf{T_i}|}{|\nabla_d \mathbf{R_i}|} \tag{16}$$

where $\mathcal{R}(\mathbf{T},\mathbf{R})$ is the structure discrepancy of $\mathbf{T}$ and $\mathbf{R}$. In Equation (16), the penalty term $|\nabla_d T_i|$ can be used to control the strength of the computed related structures. The solution of Equation (16) can be converted to:

$$\text{argmin}_{\mathbf{T},\mathbf{R}} \quad \begin{aligned} &\alpha_t \widetilde{\mathcal{R}}(\mathbf{T},\mathbf{R},\varepsilon_t,\varepsilon_r)+\beta_t\|\mathbf{T}\text{-}\mathbf{T_0}\|_2^2 \\ &+\alpha_r \widetilde{\mathcal{R}}(\mathbf{P},\mathbf{T},\varepsilon_r,\varepsilon_t)+\beta_r\|\mathbf{R}\text{-}\mathbf{R_0}\|_2^2 \end{aligned} \tag{17}$$

where α_t, α_r, β_t, and β_r are the non-negative constants which are used to balance the corresponding terms. $\|\cdot\|_2$ represents the $\updownarrow_2$ norm. The $\updownarrow_2$ norm in the above equation can be used to avoid the trivial solution through constraining $\mathbf{T}$ and $\mathbf{R}$ not to widely deviate from the input $\mathbf{T}_0$ and $\mathbf{R}_0$, respectively. The filtered image $\mathbf{T}$ can be obtained by solving:

$$\text{argmin}_t \frac{\alpha_t}{\beta_t}\mathbf{t}^T\big(\sum_{d\in\{h,v\}} \mathbf{D}_d^T\mathbf{Q}_d^{(k)}\mathbf{P}_d^{(k)}\mathbf{D}_d\big)\mathbf{t} + \|\mathbf{t}\text{-}\mathbf{t_0}\|_2^2 \tag{18}$$

where (k) expresses the kth computing of iteration. $\mathbf{Q}_d, \mathbf{P}_d, \mathbf{D}_d$ are the initialization parameters of the MuGIF. The detail map of the input CBCT image is computed by:

$$I_d = I_{VSE} - \mathbf{T}(I_{VSE}) \tag{19}$$

The final enhanced result is determined by:
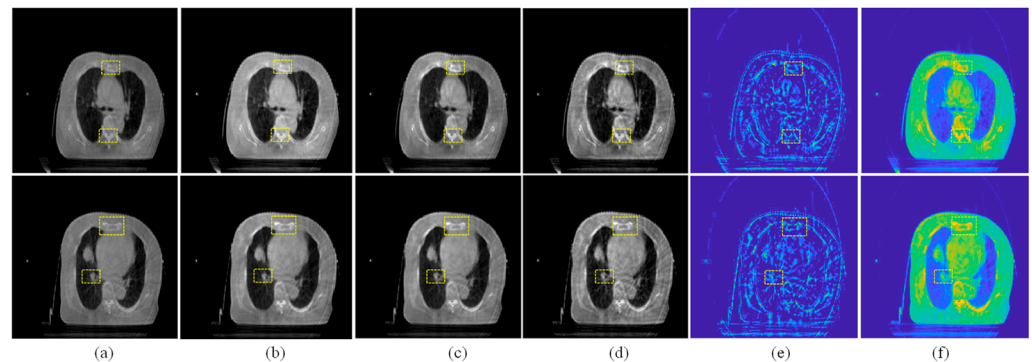
$$I_E(i,j) = I_{VSE}(i,j) + I_d(i,j) \tag{20}$$

Figure 5. Examples of Enhancement. (**a**) Source CBCT image. (**b**) I_D of (**a**). (**c**) I_{VSE} of (**a**). (**d**) Final enhanced result of (**a**). (**e**) I_d. (**f**) Difference map between (**a**,**d**).

Figure 5e gives the detail map I_d, which mainly contains the structural and textural information. Figure 5f is the difference map between the input CBCT image and the enhanced CBCT image, showing that the salient region and the imaging region of the input image are enhanced with details and textures.

3. Experiments and Analysis

3.1. Dataset and Experimental Setting

The experimental data are shown in Figure 6, and all of them are acquired from the Affiliated Hospital of Yunnan University, decrypted, and anonymized. Both CBCT and CT images are acquired for each sample of the same patient. The CBCT images were obtained by linac (XVI, Elekta Solutions AB, Stockholm, Sweden), and the corresponding CT images were acquired by Philips Brilliance Big Bore CT equipment, with a slice thickness of 3 mm. All images in our experiment were resized to 256×256 pixels. For this work, we have acquired CBCT and CT image sequences of three patients, totaling 120 pairs of images. Since there is little difference between the different sequence images of the same patient, four sections with large differences were selected as experimental data for analysis.
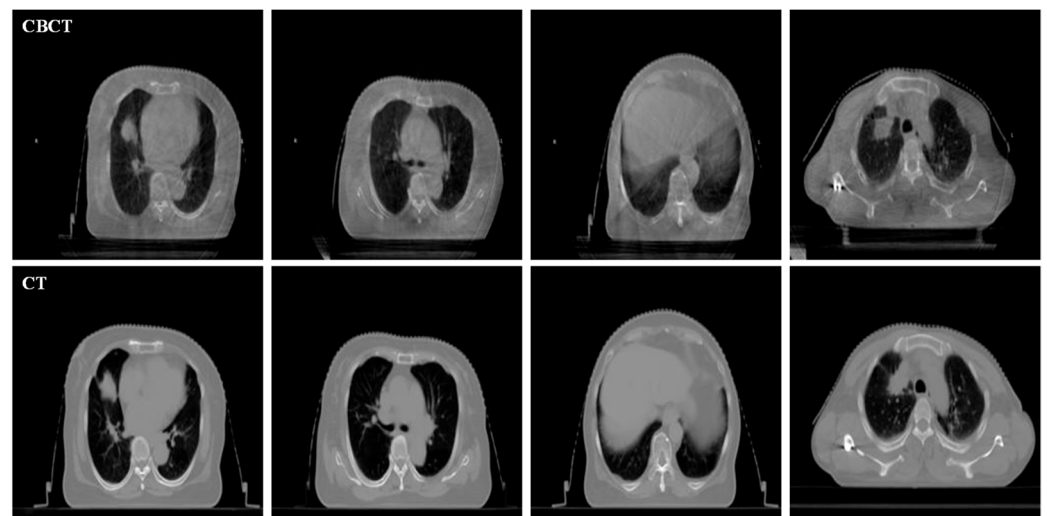
Figure 6. Experimental data. The first line is CBCT and the second line is the corresponding CT.

To illustrate the superior performance of the proposed enhancement algorithm, six classical and effective enhancement algorithms are used for comparison in our experiment, including the multi-scale retinex (MSR) method [33], the multi-scale retinex with color restoration (MSRCR) method [19], the dark channel prior (DCP) method [17], the color balance and fusion (CBF) method [34], the robust retinex model (RRM) [35], and statistical methods with image processing concepts (SMIPC) [21]. For quantitative evaluation, the enhancement performance was summarized with four imaging quality evaluation metrics: average gradient (AG) [36], spatial frequency (SF) [37], edge intensity (EI) [38], and human visual system inspired quality measures (UIQM) [39]. Among them, AG represents the gradient information, and the higher the gradient value, the higher the structural contrast of the image. SF denotes the frequency information, and a higher SF value represents the more image information and abundant imaging frequency. EI is used to measure the edge intensity of a given image; the higher the EI value, the sharper and clearer the texture of the edge is. UIQM is an often-used image evaluation metric based on the human visual system for measuring the color, clarity, and contrast of the given image. We also use the structural similarity index measure (SSIM) values [40] before and after registration of CBCT and CT images to objectively measure the registration performance. The larger these metrics, the better the quality of the enhanced images. In the experiments, all the codes are used in the version provided by the corresponding authors, and the parameters are set the same as the authors. All the experiments are performed under the Matlab R2020a, on a PC with an AMD Ryzen 7, 16 G RAM, and a 3.2 GHz processor.

3.2. Subjective Comparison and Analysis

The visual comparison of different enhancement algorithms is shown in Figures 7–10. Figure 7a is the source CBCT image, and Figure 7b is the image enhanced by MSR, which shows that the brightness of the source image is improved but with low contrast. Figure 7c,f,g show similar enhanced results with improved brightness but lacking in details. The DCP method improves the contrast of the source image, but does not enhance the details. As shown in Figure 7e, the CBF-based method shows good detail, but it still contains some noise. Compared with these methods, the proposed method shows better visual effects with higher contrast and richer detail, and the important regions are more significant.

Another three sets of experiments are shown in Figures 8–10. As can be seen from the enlarged regions and the yellow arrows in Figure 8, it is difficult to directly observe the presence of skeletal information at this position from the enlarged region in Figure 8a. The enhancement results of the comparison methods also did not improve the visual contrast in this region, but the skeletal information can be clearly observed in our result, which

means our results outperform the comparison algorithms in terms of detail, contrast, and visualization effect.
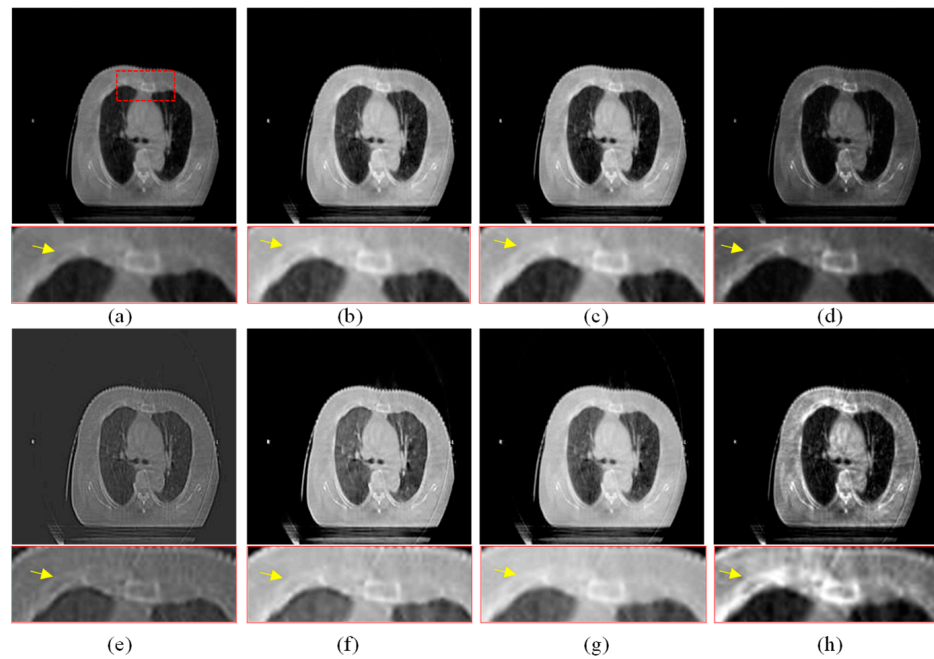

Figure 7. Enhanced results of pair 1. (**a**) Source CBCT images. (**b**) MSR. (**c**) MSRCR. (**d**) DCP. (**e**) CBF. (**f**) RRM. (**g**) SMIPC. (**h**) Ours.
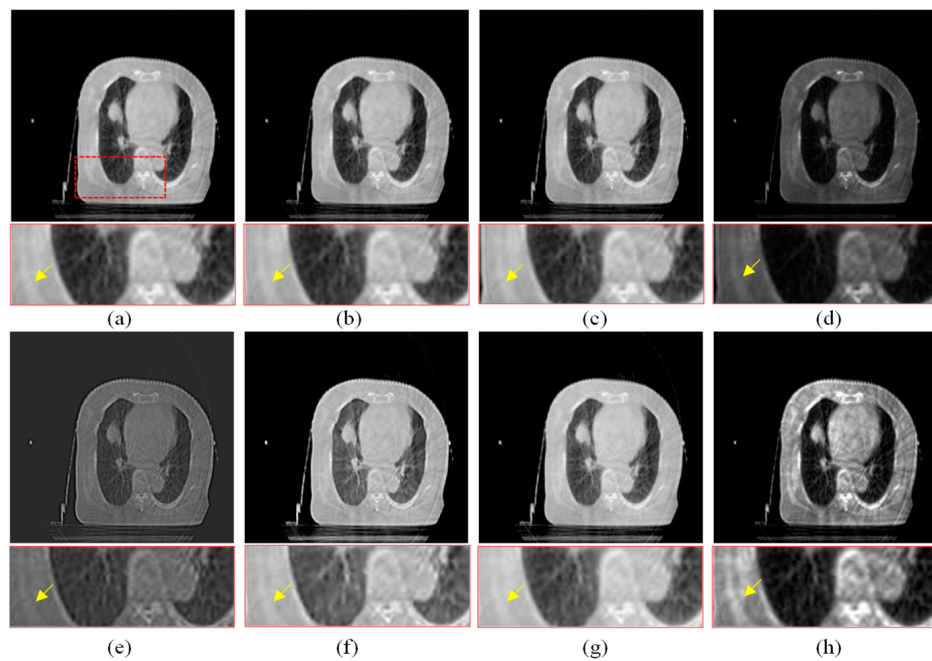
Figure 8. Enhanced results of pair 2. (**a**) Source CBCT images. (**b**) MSR. (**c**) MSRCR. (**d**) DCP. (**e**) CBF. (**f**) RRM. (**g**) SMIPC. (**h**) Ours.
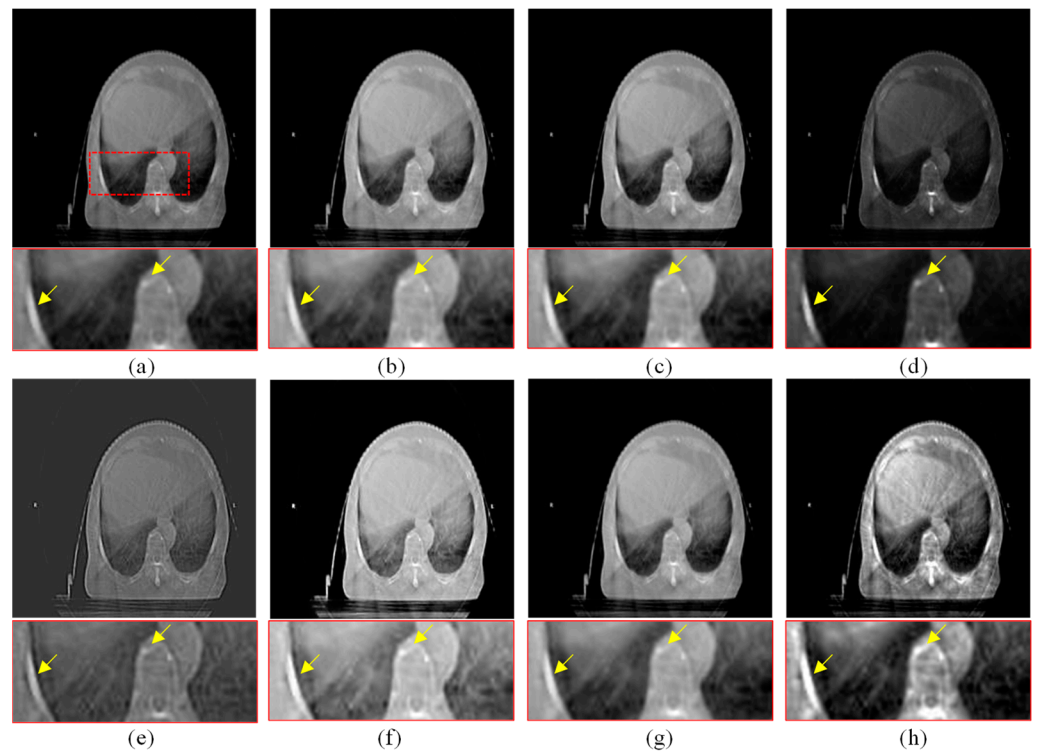
Figure 9. Enhanced results of pair 3. (**a**) Source CBCT images. (**b**) MSR. (**c**) MSRCR. (**d**) DCP. (**e**) CBF. (**f**) RRM. (**g**) SMIPC. (**h**) Ours.
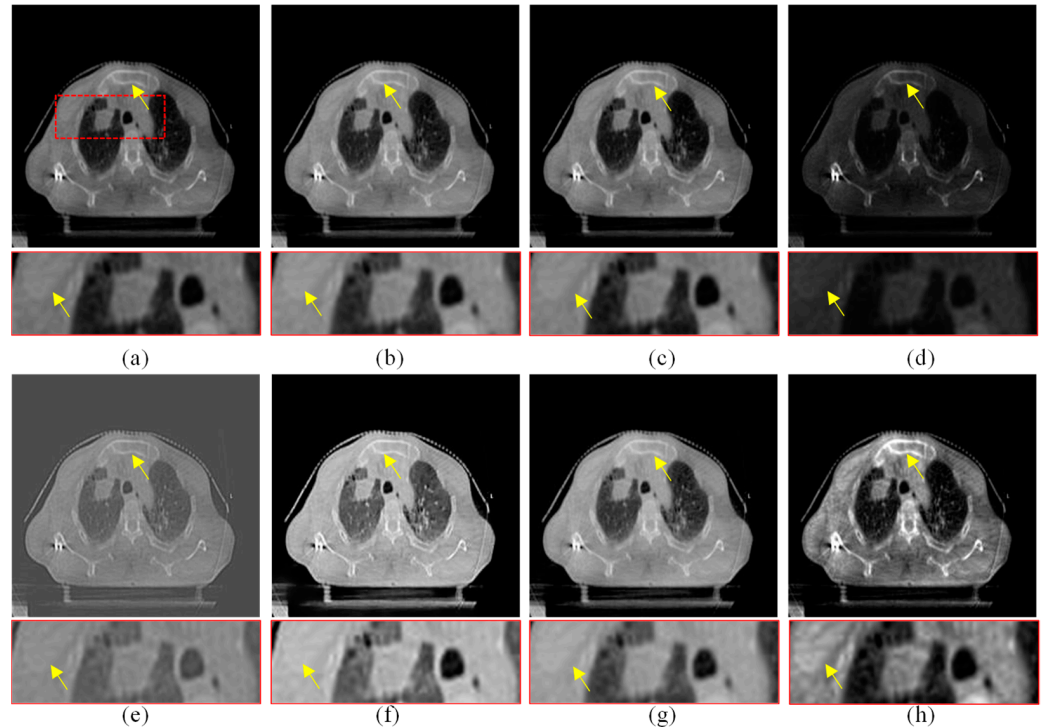
Figure 10. Enhanced results of pair 4. (**a**) Source CBCT images. (**b**) MSR. (**c**) MSRCR. (**d**) DCP. (**e**) CBF. (**f**) RRM. (**g**) SMIPC. (**h**) Ours.

The same conclusion can also be obtained in Figures 9 and 10. Especially in the enalrged region in Figure 10, our results provide a much clearer organizational structural and edge infromation, which is very helpful for disease diagnosis and treatment. Through comparison, it can be found that the rigidity informaiton in our results is more significant,

the tissue edge in our results is clearer, and the contrast of the texture structure is also better than that of the comparison algorithms. The observation effect is greatly improved by our enhancement method, proving that our method can effectively enhance the CBCT images.

3.3. Quantitative Analysis

Tables 1–4 show the evaluation metrics of different methods on Pair 1 to Pair 4. The best results in these tables are highlighted in bold and the second-best results are highlighted in bold and italic. The proposed enhancement algorithm gives the best values of AG and EI on three image pairs and four of the second-best values of SF on all images. The average evaluation metrics on all the testing images of different methods are given in Figure 11. The proposed algorithm gives the best scores for AG and EI and the second-best scores for SF and UIQM. This means the enhancement results of the proposed algorithm contain more detailed texture and gradient information and are more consistent with the human visual system. The evaluation metrics in Tables 1–4 also prove the superiority of the proposed method, which is consistent with the conclusion obtained by the visual comparison.

Table 1. Quantitative metrics of different methods on pair 1.

Method	AG	SF	EI	UIQM
MSR	4.4690	14.3406	41.3963	1.7695
MSRCR	4.3526	14.3373	40.4904	1.7174
DCP	3.0656	9.4439	27.2513	1.8540
CBF	3.7935	11.6488	30.5138	2.1783
RRM	5.4507	18.6302	48.4082	2.0375
SMIPC	4.7708	15.2181	43.5509	1.7413
Proposed	5.8681	16.1921	53.3944	1.9741

Table 2. Quantitative metrics of different methods on pair 2.

Method	AG	SF	EI	UIQM
MSR	4.5997	14.8567	43.1076	1.7329
MSRCR	4.4881	14.8235	42.2025	1.6932
DCP	3.0383	9.3338	27.2469	1.8556
CBF	4.0720	12.3792	32.8049	2.2907
RRM	5.5267	18.9434	49.7821	1.9529
SMIPC	4.8789	15.6855	45.0936	1.7019
Proposed	5.9509	16.1871	54.7970	2.0232

Table 3. Quantitative metrics of different methods on pair 3.

Method	AG	SF	EI	UIQM
MSR	3.6001	12.5238	33.6119	1.4794
MSRCR	3.4437	12.2078	32.3220	1.4792
DCP	2.3504	8.0239	20.6858	1.6847
CBF	3.5567	11.7906	28.6938	2.0258
RRM	5.0072	18.7826	44.6839	1.6157
SMIPC	4.0578	13.9605	36.8604	1.4853
Proposed	5.2918	15.1418	48.3878	1.8852

Table 4. Quantitative metrics of different methods on pair 4.

Method	AG	SF	EI	UIQM
MSR	4.2137	12.2069	38.8824	1.8911
MSRCR	3.9836	11.6625	36.8797	1.8193
DCP	2.4708	8.1086	21.4251	2.2053
CBF	3.3751	9.5269	28.0610	2.1004
RRM	6.4005	19.8617	56.1125	2.2311
SMIPC	4.7916	13.7912	43.5426	1.9177
Proposed	6.0518	15.3863	54.7559	2.1374
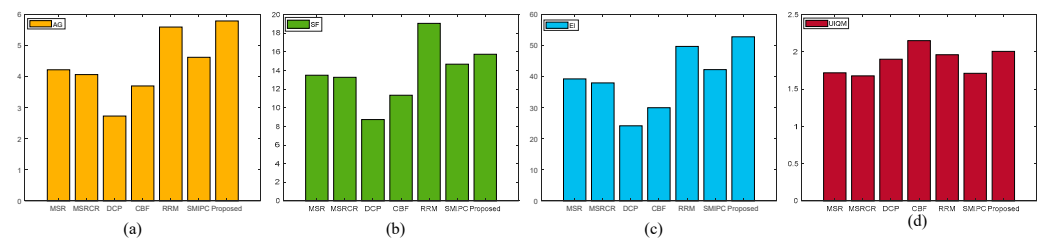
Figure 11. Comparison of the average quantitative metrics of different methods. (**a**) AG. (**b**) SF. (**c**) EI. (**d**) UIQM.

4. Support for CBCT and CT Registration in IGRT

In this section, the registration results between the source CBCT and CT images and between the CBCT images enhanced using different enhanced algorithms and CT images are compared and analyzed. In this experiment, all the registration results are obtained by the same registration model [39]. In addition to visual analysis, we also give the SSIM values before and after the registration of these images to objectively measure the registration performance.

As shown in Figure 12, Figure 12a is the unregistered source CBCT and CT images. The SSIM value of the source images is 0.5532, and it can be seen from Figure 12a that the imaging position and size of the source CBCT and CT images are different. Figure 11b is the registration result by the source CBCT and CT, and the SSIM value is 0.7184 if the CBCT image is used directly for the registration task. In the enlarged image, the edge regions are not exactly aligned in Figure 12b. Except for the CBF enhancement method, the registration accuracy was improved after CBCT images were enhanced by other methods. For example, in Figure 12c, the SSIM value is 0.7486 by registering the MSR-enhanced CBCT and CT images, which shows improved accuracy of non-enhanced CBCT and CT registration. In other words, the enhancement of CBCT images is helpful to improve the registration accuracy of CBCT and CT, which is very critical and meaningful for IGRT.

From the yellow arrows, it can be seen that our method's results have the highest registration accuracy and achieve the best SSIM value of 0.7729. In the enlarged image, it can be seen that the proposed method outperforms the comparison methods in the registration accuracy of the edge regions. This is because the proposed method enhances the saliency features, which plays a key role in the registration process. In addition, since the proposed method includes the denoising step, the noise points on the edges of image that may affect the registration were filtered out, which also helps to improve the registration accuracy.
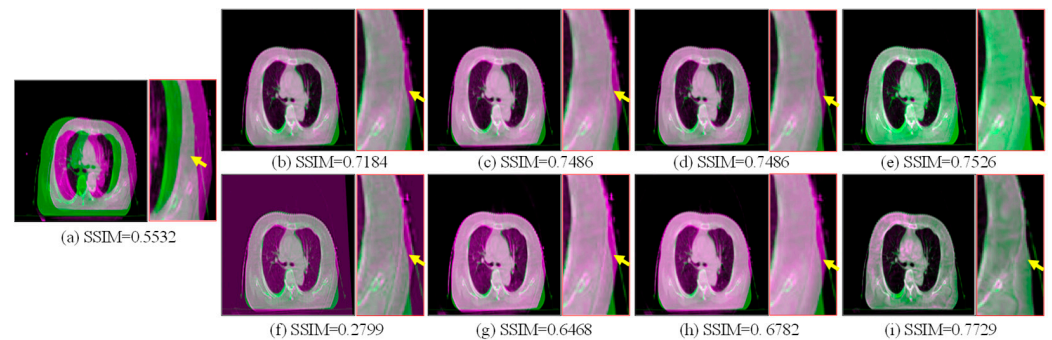
Figure 12. Registration comparison. The positions of the two images are shown in different colors. (**a**) Source CBCT and CT images. (**b**) Registration results of source CBCT and CT images. (**c**) Registration results of MSR-enhanced CBCT and CT. (**d**) Registration results of MSRCR-enhanced CBCT and CT. (**e**) Registration results of DCP-enhanced CBCT and CT. (**f**) Registration results of CBF-enhanced CBCT and CT. (**g**) Registration results of RRM-enhanced CBCT and CT. (**h**) Registration results of SMIPC-enhanced CBCT and CT. (**i**) Registration results of CBCT and CT enhanced by our method.

5. Conclusions

We propose a novel adaptive visual saliency feature enhancement algorithm of CBCT images for IGRT in this paper. Firstly, to overcome the influence of the potential noise on the image enhancement and registration, we propose a structural similarity-based low-rank approximation (SSLRA) model. SSLRA can effectively enhance the structure and gradient information of the source image while denoising it. To improve the detail in important regions, we propose a visual saliency feature enhancement (VSFE) method. The main advantage of our VSFE method is that the saliency regions are enhanced first rather than enhancing the whole image directly; in this way, the problem of insufficient visual contrast caused by manipulating the whole image is avoided. Experimental results show that the SSIM value can be increased by 0.2197 using the proposed CBCT enhancement method. It also proves that the proposed algorithm outperforms other enhancement algorithms both in visual and objective evaluations for CBCT images. In addition, it is worth noting that the proposed method is more able to support the registration task of CBCT and CT images in IGRT, which is very critical and meaningful for IGRT tasks.

Author Contributions: Conceptualization, L.X. and K.H.; methodology, L.X. and K.H.; software, L.X.; validation, and D.X.; supervision, D.X.; project administration, D.X.; funding acquisition, D.X. All authors have read and agreed to the published version of the manuscript.

Institutional Review Board Statement: Not applicable.

Informed Consent Statement: Not applicable.

Data Availability Statement: Not applicable.

Conflicts of Interest: The authors declare no conflict of interest.

References

1. Luo, Y.; Niu, T.; Jia, X.; Vela, P.A.; Zhu, L.; Tanenbaum, A.R. Joint CT/CBCT deformable registration and CBCT enhancement for cancer radiotherapy. *Med. Image Anal.* **2013**, *17*, 387–400.
2. Kidar, H.S.; Azizi, H. Enhancement of Hounsfield unit distribution in cone-beam CT images for adaptive radiation therapy: Evaluation of a hybrid correction approach. *Phys. Med.* **2020**, *69*, 269–274. [CrossRef]
3. Choi, Y.; Jang, Y.J.; Kim, K.B.; Bahng, J.; Choi, S.H. Characterization of Tissue Equivalent Materials Using 3D Printing for Patient-Specific DQA in Radiation Therapy. *Appl. Sci.* **2022**, *12*, 9768. [CrossRef]
4. Zachiu, C.; De Senneville, B.D.; Tijssen, R.H.; Kotte, A.N.; Houweling, A.; Kerkmeijer, L.; Lagendijk, J.; Moonen, C.; Ries, M. Non-rigid CT/CBCT to CBCT registration for online external beam radiotherapy guidance. *Phys. Med. Biol.* **2017**, *63*, 015027. [CrossRef] [PubMed]
5. Martin, C.; Gros, S.; Kron, T.; Wood, T.J.; Vassileva, J.; Small, W.; Min, U.N. Factors Affecting Implementation of Radiological Protection Aspects of Imaging in Radiotherapy. *Appl. Sci.* **2023**, *13*, 1533. [CrossRef]
6. Xu, X.G. An exponential growth of computational phantom research in radiation protection, imaging, and radiotherapy: A review of the fifty-year history. *Phys. Med. Biol.* **2014**, *59*, R233. [CrossRef]
7. Holmberg, O.; Malone, J.; Rehani, M.; McLean, D.; Czarwinski, R. Current issues and actions in radiation protection of patients. *Eur. J. Radiol.* **2010**, *76*, 15–19. [CrossRef]
8. Khong, P.L.; Ringertz, H.; Donoghue, V.; Frush, D.; Rehani, M.; Appelgate, K.; Sanchez, R. ICRP publication 121: Radiological protection in paediatric diagnostic and interventional radiology. *Ann. ICRP* **2013**, *155*, 380–387. [CrossRef]
9. Gianrico, S. Cone-Beam Computed Tomography and the Related Scientific Evidence. *Appl. Sci.* **2022**, *12*, 7140.
10. Xie, L.; He, K.; Gong, J.; Xu, D. Multi-Intensity Optimization-Based CT and Cone Beam CT Image Registration. *Electronics* **2022**, *11*, 1862. [CrossRef]
11. Gong, J.; He, K.; Xie, L.; Xu, D.; Yang, T. A Fast Image Guide Registration Supported by Single Direction Projected CBCT. *Electronics* **2022**, *11*, 645. [CrossRef]
12. Hung, S.; Xiao, Y.; Li, H.; Li, D.; Xiao, Y.; Li, H.; Li, D. Research on improving radiotherapy accuracy based on Image-guided radiotherapy. *Contrast Media Mol. Imaging* **2022**, *2022*, 9696403. [CrossRef]
13. He, K.; Tao, D.; Xu, D. Adaptive colour restoration and detail retention for image enhancement. *IET Image Process.* **2021**, *15*, 3685–3697. [CrossRef]
14. Liu, R.; Ma, L.; Wang, Y.; Zhang, L. Learning converged propagations with deep prior ensemble for image enhancement. *IEEE Trans. Image Process.* **2018**, *28*, 1528–1543. [CrossRef]
15. de Araujo, A.F.; Constantinou, C.E.; Tavares, J.M.R. New artificial life model for image enhancement. *Expert Syst. Appl.* **2014**, *41*, 5892–5906. [CrossRef]
16. Yelmanova, E.S.; Romanyshyn, Y.M. Medical image contrast enhancement based on histogram. In Proceedings of the 2017 IEEE 37th International Conference on Electronics and Nanotechnology (ELNANO), Kyiv, Ukraine, 18–20 April 2017; pp. 273–278.
17. He, K.; Sun, J.; Tang, X. Single image haze removal using dark channel prior. *IEEE Trans. Pattern Anal. Mach. Intell.* **2010**, *33*, 2341–2353.
18. Jobson, D.J.; Rahman, Z.; Woodell, G.A. Properties and performance of a center/surround retinex. *IEEE Trans. Image Process.* **1997**, *6*, 451–462. [CrossRef]
19. Parthasarathy, S.; Sankaran, P. An automated multi scale retinex with color restoration for image enhancement. In Proceedings of the 2012 National Conference on Communications (NCC), Kharagpur, India, 3–5 February 2012; pp. 1–5.
20. Hao, S.; Han, X.; Guo, Y.; Xu, X.; Wang, M. Low-light image enhancement with semi-decoupled decomposition. *IEEE Trans. Multimed.* **2020**, *22*, 3025–3038. [CrossRef]
21. Al-Ameen, Z. Contrast enhancement of medical images using statistical methods with image processing concepts. In Proceedings of the 2020 6th International Engineering Conference "Sustainable Technology and Development" (IEC), Erbil, Iraq, 26–27 February 2020; pp. 169–173.
22. Cassetta, M.; Stefanelli, L.V.; Pacifici, A.; Pacifici, L.; Barbato, E. How accurate is CBCT in measuring bone density? A comparative CBCT-CT in vitro study. *Clin. Implant Dent. Relat. Res.* **2014**, *16*, 471–478. [CrossRef]
23. He, K.; Zhang, X.; Xu, D.; Gong, J.; Xie, L. Fidelity-driven optimization reconstruction and details preserving guided fusion for multi-modality medical image. *IEEE Trans. Multimed.* **2022**. [CrossRef]
24. Wang, Y.; He, Q.; Luo, J. Fast randomized singular value decomposition-based clutter filtering for shear wave imaging. *IEEE Trans. Ultrason. Ferroelectr. Freq. Control* **2020**, *67*, 2363–2377. [CrossRef] [PubMed]
25. Shi, M.; Zhang, F.; Wang, S.; Zhang, C.; Li, X. Detail preserving image denoising with patch-based structure similarity via sparse representation and SVD. *Comput. Vis. Image Underst.* **2021**, *206*, 103173. [CrossRef]
26. Zeng, M.; Zhang, W.; Chen, Z. Group-based K-SVD denoising for bearing fault diagnosis. *IEEE Sens. J.* **2019**, *19*, 6335–6343. [CrossRef]
27. Guo, Q.; Zhang, C.; Zhang, Y.; Liu, H. An efficient SVD-based method for image denoising. *IEEE Trans. Circuits Syst. Video Technol.* **2015**, *26*, 868–880. [CrossRef]
28. Cong, R.; Lei, J.; Fu, H.; Cheng, M.; Lin, W.; Huang, Q. Review of visual saliency detection with comprehensive information. *IEEE Trans. Circuits Syst. Video Technol.* **2018**, *29*, 2941–2959. [CrossRef]

29. Achanta, R.; Süsstrunk, S. Saliency detection using maximum symmetric surround. In Proceedings of the 2010 IEEE International Conference on Image Processing, Hong Kong, China, 26–29 September 2010; pp. 2653–2656.

30. Ali, U.; Lee, I.H.; Mahmood, M.T. Guided image filtering in shape-from-focus: A comparative analysis. *Pattern Recognit.* **2021**, *111*, 107670. [CrossRef]

31. Xu, S.; Zhang, J.; Wang, J.; Sun, K.; Zhang, C.; Liu, J.; Hu, J. A model-driven network for guided image denoising. *Inf. Fusion* **2022**, *85*, 60–71. [CrossRef]

32. Guo, X.; Li, Y.; Ma, J. Mutually guided image filtering. In Proceedings of the 25th ACM International Conference on Multimedia, Mountain View, CA, USA, 23–27 October 2017; pp. 1283–1890.

33. Petro, A.B.; Sbert, C.; Morel, J.M. Multiscale retinex. *Image Process. On Line* **2014**, *4*, 71–88. [CrossRef]

34. Ancuti, C.O.; Ancuti, C.; De Vleeschouwer, C.; Bekaert, P. Color balance and fusion for underwater image enhancement. *IEEE Trans. Image Process.* **2017**, *27*, 379–393. [CrossRef]

35. Li, M.; Liu, J.; Yang, W.; Sun, X.; Guo, Z. Structure-revealing low-light image enhancement via robust retinex model. *IEEE Trans. Image Process.* **2018**, *27*, 2828–2841. [CrossRef]

36. Trier, O.D.; Taxt, T. Evaluation of binarization methods for document images. *IEEE Trans. Pattern Anal. Mach. Intell.* **1995**, *17*, 312–315. [CrossRef]

37. Li, S.; Kwok, J.T.; Wang, Y. Combination of images with diverse focuses using the spatial frequency. *Inf. Fusion* **2001**, *2*, 169–176. [CrossRef]

38. He, K.; Gong, J.; Xie, L.; Zhang, X.; Xu, D. Regions preserving edge enhancement for multisensor-based medical image fusion. *IEEE Trans. Instrum. Meas.* **2021**, *70*, 5008513. [CrossRef]

39. Panetta, K.; Gao, C.; Agaian, S. Human-visual-system-inspired underwater image quality measures. *IEEE J. Ocean. Eng.* **2015**, *41*, 541–551. [CrossRef]

40. Wang, Z.; Bovik, A.; Sheikh, H.; Simoncelli, E.P. Image quality assessment: From error visibility to structural similarity. *IEEE Trans. Image Process.* **2004**, *13*, 600–612. [CrossRef]